International Journal of Hydrogen Energy 106 (2025) 1403–1416

Contents lists available at ScienceDirect

International Journal of Hydrogen Energy

journal homepage: www.elsevier.com/locate/he

Coking resistant Ru supported on Sm-substituted $CaZrO_3$ catalyst for dry reforming of methane: The effect of Ru loading on catalytic activity

Leonardo Duranti [a], Umberto Pasqual Laverdura [b,*], Elisabetta Di Bartolomeo [a], Maria Luisa Grilli [b], Rosa Chierchia [b], Claudio Larosa [b], Alessio Varotto [b], Simonetta Tuti [c], Silvia Licoccia [a,d], Igor Luisetto [b,1]

[a] Department of Chemical Science and Technologies, University of Rome Tor Vergata, Via della Ricerca Scientifica, 00133, Rome, Italy
[b] Department of Energy Technologies and Renewable Sources - TERIN, ENEA C.R. Casaccia, S.P. 081 Via Anguillarese 301, 00123, S.M. di Galeria, Rome, Italy
[c] Department of Science, University of Rome "Roma Tre", Via della Vasca Navale 79, 00146, Rome, Italy
[d] NAST Centre, University of Rome Tor Vergata, Via Della Ricerca Scientifica, 00133, Rome, Italy

ARTICLE INFO

Handling Editor: Suleyman I. Allakhverdiev

ABSTRACT

Dry reforming of methane has industrially appealing advantages over other routes towards syngas production: CH_4 and CO_2 DRM conversion simultaneously tackles two main greenhouse gases to obtain a H_2/CO ratio close to unity, ideal for long-chain hydrocarbons production via Fischer-Tropsch method. Designing high-performing and stable catalysts is pivotal for long-lasting operation. Ni-supported systems are by far the most used, owing to their outstanding activity and cost-effectiveness. Nevertheless, Ni promotes carbon deposition which results in severe deactivation. Supported noble metals combine high performance to coking resistance but this comes at a high cost. Here, the effects on DRM activity of low (≤3.0 wt%) ruthenium strategical loading onto a calcium zirconate perovskite oxide were investigated. In the $CaZrO_3$, Zr substrate was partially substituted with samarium ($CaZr_{0.85}Sm_{0.15}O_{3-\delta}$, CZSm) to increase the extent of oxygen vacancies, favoring reactants adsorption on a highly basic surface. Ru was added during the perovskite synthesis to obtain RxCZSm (x = 0.5, 1.5, 3.0 wt% Ru). Structural and textural analyses revealed partial Ru inclusion in the oxide lattice leading to a net surface area increase (>50%). Different DRM activity depending on Ru oxidation state, substrate NPs coverage and reaction temperature was observed. R0.5CZSm displayed higher CH_4 conversion (97.6 %) at 850 °C, while R3.0CZSm outperformed the lower Ru-loaded compounds at 550 °C, showing an H_2/CO ratio of 0.77. Durability tests revealed high stability of all RxCZSm catalysts, with no carbon deposition. Low Ru loading on a tailored oxide substrate is an effective alternative for active and durable DRM catalysts.

1. Introduction

The European Union (EU) has set ambitious goals for the reduction of greenhouse gases emissions to rapidly reach economic independence from the intensive exploitation of fossil fuels. The EU Strategic Energy Technology Plan (SET Plan) outlines the priorities and actions needed to achieve such targets. The key factor for the transition towards a climate-neutral or negative system is the implementation of low-carbon technologies [1]. Developing reliable and high-performing dry reforming of methane reaction (DRM) is a promising way to address the *actions* objectives stated in the EU's SET Plan, allowing for faster integration of renewables within the energy system and increasing energy efficiency of industrial processes.

DRM process (1) converts methane and carbon dioxide, both major greenhouse gases, into syngas, a mixture of carbon monoxide and hydrogen.

$$CH_4 + CO_2 \rightarrow 2CO + 2H_2 \quad \Delta H^0 = 247.3\ kJ\,/\,mol \tag{1}$$

Having the proper H_2/CO ratio, the syngas can be used to produce various fuels such as dimethyl ether or long-chain hydrocarbons in Fischer-Tropsch process [2–4]. Electrical energy can be also directly obtained from syngas if it is exploited as fuel in solid oxide fuel cells [5–7]. Many studies have been focused on the design of novel catalysts and reactors implementing DRM, since it represents a greener solution

* Corresponding author.
E-mail address: umberto.pasqual@enea.it (U.P. Laverdura).
[1] Untimely passed away.

https://doi.org/10.1016/j.ijhydene.2025.01.366
Received 18 November 2024; Received in revised form 17 January 2025; Accepted 23 January 2025
0360-3199/© 2025 The Authors. Published by Elsevier Ltd on behalf of Hydrogen Energy Publications LLC. This is an open access article under the CC BY license (http://creativecommons.org/licenses/by/4.0/).

with respect to the conventional syngas sources [8–16]. Compared to the steam methane reforming (SMR) (2) or to the autothermal reforming (ATR), a combination of SMR and catalytic partial oxidation of methane (CPOM) (3), the DRM is the most endothermic process:

$$CH_4 + H_2O \rightarrow CO + 3H_2 \quad \Delta H^0 = 206.8\ kJ\ /\ mol \tag{2}$$

$$CH_4 + \frac{1}{2}O_2 \rightarrow CO + 2H_2 \quad \Delta H^0 = -36\ kJ\ /\ mol \tag{3}$$

This is due to the higher stability of CO_2 as oxidizing agent, compared to water or oxygen; anyways, the DRM reaction is thermodynamically favored at temperatures compatible with standard SOFC operation, thus making the coupling of the two systems beneficial.

Concomitant and unwanted side reactions take place alongside DRM, such as reverse water gas shift (RWGS) (4), which partially consumes the produced hydrogen reducing the overall H_2/CO ratio, the methane cracking (5) and the Boudouard reaction (6), which are directly involved in the formation of various carbonaceous deposits, responsible for the deactivation of the DRM catalyst, both at higher temperature (methane cracking) and at lower temperature (Boudouard reaction) [9]:

$$CO_2 + H_2 \rightarrow CO + H_2O \quad \Delta H^0 = 41.2\ kJ\ /\ mol \tag{4}$$

$$CH_4 \rightarrow C + 2H_2 \quad \Delta H^0 = 75\ kJ\ /\ mol \tag{5}$$

$$2CO \rightarrow C + CO_2 \quad \Delta H^0 = -171.0\ kJ\ /\ mol \tag{6}$$

Noble metals, such as rhodium, platinum and palladium, have shown high activity and selectivity for DRM, due to their ability to adsorb and activate both methane and carbon dioxide [17–19], although the high cost prevents their widespread utilization. Among the less expensive transition metals, only Ni showed comparable activity towards DRM. On the other hand, Ni suffers from rapid deactivation due to sintering over prolonged operation and, most crucially, coking [20,21].

The choice of a suitable DRM catalyst depends on various factors other than activity, cost, and availability of the metal, such as selectivity and stability over time, according to the specific application. Ru is a well-known catalyst for DRM, as it can promote the activation of both methane and carbon dioxide on its surface, being also the cheapest among noble metals [22–24]. Unlike the more commonly used nickel-based catalysts, ruthenium has a higher resistance to coking and prevents the formation of carbon whiskers, which are the principal cause of nickel-based catalysts fast deactivation at higher temperatures [20, 25–27]. Recently developed systems with supported or substitutional Ru have shown remarkable and stable performance for DRM [28–30]. Furthermore, the exsolution of Ru nanoparticles from a Ru containing fluorite oxide structure ($Sm_2Ru_{0.2}Ce_{0.8}O_7$) was proven to ensure 70% CH_4 conversion at 700 °C and a H_2/CO ratio of 0.85, together with coking resistance for over 100 h operation [31].

Catalyst supports include perovskite-based materials with ABO_3 structure [32], such as zirconates $AZrO_3$ (A = Ca, Sr, Ba) [33–35], which have attracted considerable attention due to their unique physico-chemical properties: relatively large surface area, thermal and redox stability, and surface basicity to favor carbon dioxide adsorption [36]. $CaZrO_3$, $SrZrO_3$ and $BaZrO_3$ compounds have also been largely studied for proton-conducting fuel cells materials [37–41]. As reported by Wu et al. [42], the presence of oxygen vacancies increases the formation of adsorbed oxygen species and their mobility due to the oxygen imbalance on the catalyst support surface: this aspect, crucial for highly O^{2-} conducting oxides [43], has the overall effect of promoting the anti-coking properties [25]. To this extent, samarium inclusion within the support lattice up to 20 mol% was reported to increase the amount of oxygen vacancies, enhancing coking resistance both in fluorite [44] and perovskite oxides [45]. Another advantage of using such perovskite oxides as support is the possible implementation on the anode side of a SOFC in Indirect Internal Reforming (IIR) configuration, since the physical-chemical characteristics are compatible with SOFC anodic materials [46]. The thermal stability of the ceramic catalyst support is directly related to the high endothermicity of DRM reaction: under these conditions, significant local cooling can result in the failure of the ceramic component [47]. In this respect, zirconates have also the advantage of a better mechanical resistance over other rare-earth-based mixed perovskite oxides [48].

Table 1
– Stoichiometry and labels used in the following for each sample. For RxCZSm samples, elemental composition obtained by Energy Dispersive X-Ray analysis is also reported.

Sample Label	Sample stoichiometry	Elemental composition of Ru-containing samples			
		Ca (mol %) on Ca site	Zr (mol %) on Zr site	Sm (mol%) on Zr site	Ru (wt %)
CZ	$CaZrO_{3-\delta}$				
CZSm	$CaZr_{0.85}Sm_{0.15}O_{3-\delta}$				
R0.5CZSm	0.5 wt% Ru–$CaZr_{0.85}Sm_{0.15}O_{3-\delta}$	94 ± 1	88.0 ± 0.3	15 ± 2	0.5 ± 0.1
R1.5CZSm	1.5 wt% Ru–$CaZr_{0.85}Sm_{0.15}O_{3-\delta}$	97 ± 6	85 ± 6	14 ± 2	1.7 ± 0.3
R3.0CZSm	3.0 wt% Ru–$CaZr_{0.85}Sm_{0.15}O_{3-\delta}$	96 ± 6	81 ± 6	15 ± 2	3.1 ± 0.3

Aim of this work is to design an efficient and stable catalyst for the dry reforming of methane, active in the 550 °C–850 °C temperature range, able to operate in a wide range of operational conditions. Ruthenium supported on a calcium zirconate mixed oxide in which 15 mol% of Zr is replaced by samarium at the B-site (Ru_X-$CaZr_{0.85}Sm_{0.15}O_{3-\delta}$) is proposed as DRM catalyst. Zr substitution with Sm results in the perovskite oxide lattice distortion and introduces a large extent of oxygen vacancies. To achieve the highest degree of phase purity, ensuring at the same time a high specific surface area, the glycine solution combustion synthesis route was chosen. As a matter of fact, this method ensures pure perovskite crystal formation with little-to-none amounts of secondary phases [3,49–51]. Moreover, the use of glycine as fuel has the advantage of increasing the final surface area of the catalyst as compared to other commonly used fuels. The ruthenium nitrosyl nitrate precursor was directly added during the perovskite support synthesis, as this procedure has been observed to ensure a fine dispersion of the active catalyst onto the oxide support [44,52]. The interaction between Ru and $CaZr_{0.85}Sm_{0.15}O_3$ improved the dispersion and stability of Ru, allowing for a finer control over the particle size of the catalyst, also reducing the sintering effect, which is a crucial aspect in high-temperature applications. The effect of varying the amount of supported ruthenium (0.5, 1.5 and 3.0 wt%) was evaluated on the catalytic activity and catalyst stability.

2. Materials and methods

2.1. Catalysts synthesis

The *x* wt.% Ru–$CaZr_{0.85}Sm_{0.15}O_{3-\delta}$ (x = 0.5, 1.5 and 3.0) catalyst samples were prepared by the solution combustion method [3] using glycine (NH_2CH_2COOH) (Aldrich, ≥99%) as fuel for the following oxidants: $Ca(NO_3)\bullet 4H_2O$ (Aldrich, 99.95%), $ZrO(NO_3)\bullet 6H_2O$ (Aldrich, 99.99%), $Sm(NO_3)_3\bullet 6H_2O$ (Aldrich, 99.999%) and $Ru(NO)(NO_3)_3$ (Thermo Scientific Chemicals). The NO_3^-:glycine ratio was set at 1.15. The reagents were dissolved in a minimal amount of H_2O and heated to 80 °C to promote the formation of a gel. The temperature was then rapidly increased to 250 °C and the combustion was ignited by a vigorous flame with the subsequent formation of voluminous ashes. XRD

analysis reported representatively for R3.0CZSm sample in Fig. S1a revealed that the ashes were not fully crystalline and TGA analysis in flowing air of Fig. S1b showed that residual water desorption, nitrates and carbonates decomposition ended at 800 °C. To obtain a pure phase while ensuring suitable surface area, the ashes were calcined at 850 °C for 5 h. The same synthesis route was followed for the Ru-free Sm-substituted $CaZr_{0.85}Sm_{0.15}O_{3-\delta}$ and for the Sm-free $CaZrO_{3-\delta}$ oxide supports.

Energy Dispersive X-ray analyses (EDX) were performed on the R_xCZSm (x = 0.5, 1.5 and 3.0 wt%) samples using an INCAx-sight, Model: 7426 apparatus, by Oxford Instruments. An acceleration voltage of 20 kV was employed and five different sites were measured for each sample. In Table 1 the labels for the samples used in this work are reported, together with the averaged elemental compositions, that resulted very close to the nominal values.

To investigate the effects of the exposure to reducing conditions, all samples were subjected to a reducing treatment in 100 ml/min of 5% H_2/Ar at 850 °C for 10 h.

2.2. Catalyst characterization

X-ray powder diffraction patterns were recorded using a Philips X'Pert Pro 500 diffractometer equipped with a Cu Kα (λ = 1.5418 Å) source and the Bragg-Brentano θ–θ configuration in the 10°–80° 2θ range, with 0.01° step size and 2 s acquisition time.

Thermogravimetric analyses (TGA) were performed using a Mettler Toledo TG-DSC 1 Star System. 25 mg of samples were loaded in platinum crucibles and the mass variation was monitored upon heating. TGA analysis was performed on RxCZSm precursor ashes to select the proper calcination temperature. For this purpose, 100 ml/min air flux was used up to 1000 °C with a 10 °C/min heating ramp, with no sample pre-treatment. TGA was also used to assess the relative amount of oxygen vacancies of CZ and CZSm. The measurement was performed in 100 ml/min N_2 flux up to 1000 °C, with a 10 °C/min heating ramp. A pre-treatment step at 100 °C for 1 h was applied prior to the measurement, to ease adsorbed water release. Finally, to evaluate the amount of possibly formed carbonaceous deposits after the time on stream stability experiment, the spent mixture of RxCZSm catalysts and silicon carbide (SiC), used for catalytic tests, was collected from the bed reactor and sieved with a 25 μm sieve to exclude most of the SiC. Thus obtained RxCZSm samples were put in a Pt crucible and the mass variation was monitored upon heating in 100 ml/min air flux up to 1000 °C, with a 10 °C/min heating ramp. No pre-treatment was performed on spent RxCZSm samples. A correction for buoyancy effect was applied in all TGA experiments.

N_2 adsorption/desorption isotherms were measured at −196 °C using an adsorption apparatus ASAP 2020 from Micromeritics. Samples were degassed at 350 °C under vacuum for 4 h prior to the analysis. Specific surface area (SSA) was determined using the Brunauer-Emmett-Teller method (BET) in the linear range of relative pressure (p/p^0) of 0.07–0.3. The pore–size distributions were calculated from the desorption branches using the Barrett–Joyner–Halenda (BJH) model. The total pore volume was estimated to be the liquid N_2 volume at relative pressure p/p^0 of 0.95.

Temperature-programmed reduction (H_2-TPR) experiments were performed using a flow-through automatic instrument (AutoChem 2950 HP Micromeritics). The calcined samples were placed in a quartz reactor and pre-treated with 30 $cm^3\ min^{-1}$ of a 5% O_2/He gas mixture at 850 °C for 1 h and cooled to 50 °C. Then, 30 $cm^3\ min^{-1}$ of a 5% H_2/Ar gas mixture was introduced into the reactor and the temperature was raised to 1000 °C at a heating rate of 10 °C/min. H_2 consumption was measured using a TCD detector calibrated by reducing a known amount of CuO (99.99% purity from Sigma Aldrich).

Morphological analysis was performed with a Zeiss Leo SUPRA 35 scanning electron microscope equipped with a cold field emission electron source (FE-SEM); SmartSEM V05.04.02.00 software was used for images acquisition. Prior to the analyses, samples were dispersed with isopropyl alcohol in an ultrasonic bath and the dispersion was drop-cast onto the aluminum stubs, which were then heated at 50 °C to favor solvent evaporation.

The elemental surface composition was determined by X-ray photoelectron spectroscopy (XPS) using a VG Escalab MkII Spectrometer equipped with oil-free pumps to avoid carbon contaminations. An aluminum source (Al Kα 1486.6 eV) was employed to perform the analysis. The catalysts powders were pressed into pellets and a reference gold wire was placed on their surface to account for possible sample charging. The XPS measurement was performed in a base vacuum of 3.0×10^{-9} mbar.

2.3. DRM tests set-up

Reactions were monitored in a continuous fixed bed reactor (ID 10 mm) heated with a tubular oven equipped with a temperature controller (Carbolite Gero TS1 12/60/150). The gases were regulated by four mass flow controllers (Bronkhorst EL-Prestige). The reactor outlet was analysed every 3 s with an Advance Optima 2000 (ABB) equipped with a Peltier device to remove water, and the following systems: a) infrared detector (URAS 14) to measure CO_2 (vol%), CO (vol%) and CH_4 (vol%); b) TCD detector (Caldos 15) to measure H_2 (vol%). A catalyst amount of 200 mg was mixed with 2.00 g of silicon carbide (SiC Sigma Aldrich dp < 550 μm) and loaded into the quartz reactor to obtain a catalytic bed volume of 2.00 cm^3. A gas mixture with a total flow rate of 200 $cm^3\ min^{-1}$ was used with a specific inlet composition capable of meeting the detection limits of the ABB instrument. For the RWGS reaction, the composition of the H_2:CO_2:N_2 mixture was 20:20:60 vol% and for the DRM reaction, the composition of the CH_4:CO_2:N_2 mixture was set to 10:10:80 vol%. Under these conditions, a gas hourly space velocity (GHSV) of 60000 $cm^3\ h^{-1}\ g^{-1}$ was established. During the reaction, balance of carbon ($C_{balance}(\%)$) (eq. (7)), H_2 and CO selectivity ($S_i(\%)$) (eqs. (8) and (9)), CH_4 and CO_2 percent conversions ($X_i(\%)$) (eq.(10)–(12)), and the ratio between H_2 and CO (eq. (13)) were calculated according to the equations:

$$C_{balance}(\%) = \frac{F \bullet \sum C_i}{F^0 \bullet \sum C_i^0} \times 10^2 \tag{7}$$

$$S_{H_2}(\%) = \frac{C_{H2,out}}{C_{H2,out} + C_{CO,out}} \times 10^2 \tag{8}$$

$$S_{CO}(\%) = \frac{C_{CO,out}}{C_{H2,out} + C_{CO,out}} \times 10^2 \tag{9}$$

$$X_{CO_2}(\%) = \frac{C_{CO2,in} - C_{CO2,out}}{C_{CO2,in} + \epsilon C_{CO2,out}} \times 10^2 \tag{10}$$

$$X_{CH_4}(\%) = \frac{C_{CH4,in} - C_{CH4,out}}{C_{CH4,in} + \epsilon C_{CH4,out}} \times 10^2 \tag{11}$$

$$\in = \frac{V - V^0}{V^0} \tag{12}$$

$$\frac{H_2}{CO} = \frac{H_{2,mol\ out}}{CO_{mol\ out}} \tag{13}$$

where: C_i and C_i^0 are the molar fractions of the components in the outlet and inlet of the reactor respectively, F and F^0 are the total molar flow at the inlet and outlet of the reactor, ∈ is the expansion factor that considers the volume change during the reaction [53].

3. Results and discussion

3.1. Perovskite oxide support structural characterization

The $CaZr_{0.85}Sm_{0.15}O_{3-\delta}$ support structure was characterized and

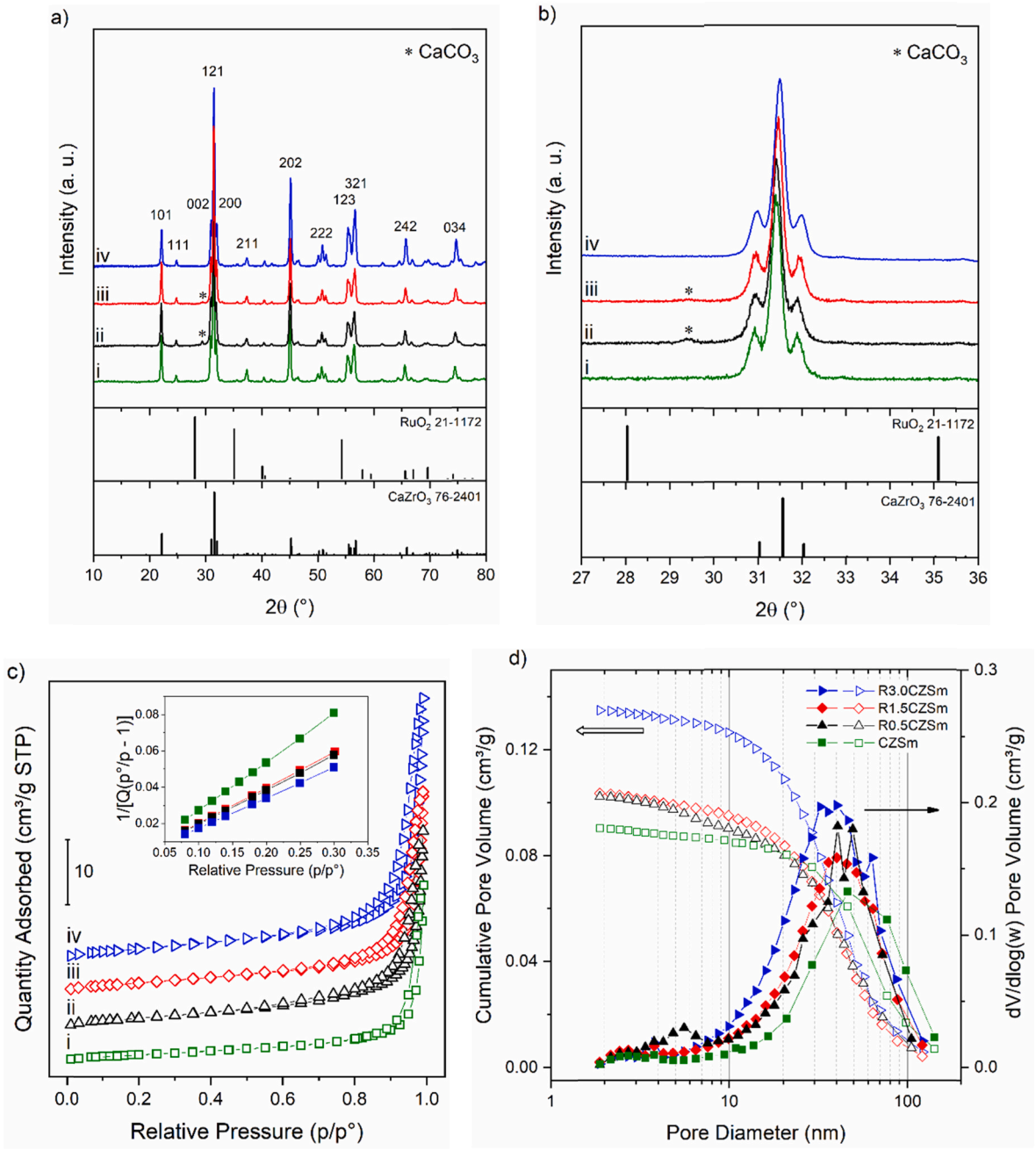

Fig. 1. – a) XRD diffraction pattern of as prepared samples: (i) CZSm; (ii) R0.5CZSm; (iii) R1.5CZSm; (iv) R3.0CZSm. Reference patterns of $CaZrO_3$ and RuO_2 are included; b) $27° < 2\theta < 36°$ magnification of a; c) N_2 adsorption and desorption isotherms of (i) CZSm, (ii) R0.5CZSm, (iii) R1.5CZSm and (iv) R3.0CZSm. The BET transform plot in the 0.07–0.3 p/p^0 range is reported in the inset; d) BJH desorption cumulative volume of pores, open symbols, and the corresponding average pore width, closed symbols.

compared to the Sm-free $CaZrO_3$ oxide. XRD patterns of as prepared CZ and CZSm, together with the Size-Strain plot are reported in Fig. S2c while the obtained structural parameters are listed in Table S1. Both diffractograms exhibit the presence of a single oxide phase for CZ and CZSm, revealing the complete inclusion of 15 mol% Sm into the CZ lattice. The diffraction peaks of CZ are indexed using *Pcmn* (62) space group symmetry with an orthorhombic structure belonging to $CaZrO_3$ (PDF 76–2401) and the obtained peak positions match those reported on the reference PDF card. For CZSm, the XRD pattern showed a shift to lower diffraction angles as compared to the $CaZrO_3$ reference. The shift of the peaks indicates that the interplanar spacing increases when 15 mol% substitutional Sm ions are present in the parent perovskite lattice. This lattice expansion is due to the substitution of Zr^{4+} B-site ions (ionic radius = 0.840 Å) with larger Sm^{3+} ions (1.132 Å) [4]. The presence of trivalent ions in the crystalline structure caused a charge imbalance that was mainly compensated by the formation of oxygen vacancies and led to a distortion of the host structure symmetry. Moreover, such a large Sm substitution resulted in a minor segregation of Ca ions, observable as a weak peak at 53.9° 2θ (* in Fig. S2a) ascribable to CaO (PDF 37–1497) [3]. The CaO secondary phase likely reacted over time with atmospheric H_2O to form $Ca(OH)_2$ and eventually with CO_2 to form stable $CaCO_3$. According to data reported in Table S1, Zr substitution with Sm resulted in a 1.6% unit cell volume increase in CZSm, a slight decrease of crystallite size D and an order of magnitude increase of inhomogeneous lattice strain ε^{S-S}, which passed from 0.57×10^{-3} for CZ to 5.7×10^{-3} for CZSm. The increased amount of oxygen vacancies introduced by Sm

Table 2
– Structural and textural parameters obtained for CZSm, R0.5CZSm, R1.5CZSm, and R3.0CZSm samples.

Sample	Lattice parameters				Size–Strain Plot			Specific Surface Area
	a (Å)	b (Å)	c (Å)	Volume (Å^3)	D (nm)	ε^{S-S} (× 10^{-3})	R^2	BET (m^2/g)
CZSm	5.613	8.057	5.787	261.69	44.2	5.70	0.999	16.35 ± 0.06
R0.5CZSm	5.614	8.052	5.779	261.24	34.6	6.57	0.991	22.92 ± 0.08
R1.5CZSm	5.603	8.043	5.778	260.39	36.8	3.52	0.999	22.28 ± 0.06
R3.0CZSm	5.599	8.033	5.773	259.64	36.8	7.68	0.994	25.98 ± 0.07

substitution was confirmed by means of thermogravimetric analysis in N_2 environment, carried out on CZ and CZSm samples. TGA results are reported in Fig. S3: both CZ and CZSm show a continuous mass decrease with increasing temperature, displaying a step-like loss around 600 °C. The former continuous loss is due to lattice oxygen progressive thermal release, the latter is likely attributable to $CaCO_3$ derived from calcium oxides impurities reaction with atmospheric CO_2, which degrades back to CaO when heated, according to Eq (14) [3].

$$CaCO_3 \rightarrow CaO + CO_2 \quad \Delta H^0 = 178.2\ kJ\,/\,mol \tag{14}$$

While for CZ the mass loss at 1000 °C is around 3.2%, it accounts for 7.3% in CZSm, indicating how 15 mol% of Sm substitution dramatically increased the amount of oxygen vacancies (steeper slope of the TGA curve up to 600 °C), and favored the formation of a larger extent of calcium-based impurities (larger loss at around 600 °C due to $CaCO_3$ decomposition).

3.2. Structural and textural properties of the Ru-supported catalysts

XRD patterns of RxCZSm samples are reported in Fig. 1a for x = 0 (CZSm), 0.5, 1.5 and 3.0 wt%. $CaZrO_3$ and RuO_2 reference PDF patterns are also present. An enlargement around the set of (002), (121) and (200) peaks, 2θ = 27°–36°, is reported in Fig. 1b, while lattice parameters and Size-Strain analysis results are reported in Table 2. Fig. 1b shows how increasing the amount of ruthenium, the CZSm pattern shifts towards higher 2θ values, reducing the unit volume cell down to 259.64 Å^3 for R3.0CZSm. The addition of Ru during CZSm synthesis did not affect the inhomogeneous lattice strain as much as the crystallite size, that showed a net decrease from the 44 nm of CZSm to 34–36 nm of RxCZSm. The most intense peaks belonging to RuO_2 (2θ = 28.04° and 2θ = 35.09°) are not observable in RxCZSm samples. Nevertheless, in Ru containing samples R0.5CZSm and R1.5CZSm the presence of $CaCO_3$ impurities (PDF 47–1743) was observed as a very low intense peak at 2θ = 29.4°. As previously observed from TGA results of Fig. S3, $CaZrO_3$ lattice alteration by 15 mol% Zr replacement with Sm increased the amount of calcium-based secondary phase [3]. Furthermore, ruthenium addition led to a further Ca ions segregation and subsequent $CaCO_3$ phase formation (weak peak in Fig. 1a) indicating how Ru cations likely entered the host perovskite lattice.

N_2 adsorption-desorption isotherms of CZSm and RxCZSm samples are shown in Fig. 1c, while BJH cumulative pore volume obtained from the desorption branch of the isotherms is reported in Fig. 1d, together with the corresponding average pore width. BET specific surface area values are reported in Table 2. According to the International Union of Pure and Applied Chemistry (IUPAC) classification, the isotherms belong to a Type II, typical of macroporous materials with unrestricted multilayer adsorption [54]. A 40% increase of SSA was observed for R0.5CZSm and R1.5CZSm, going from 16.4 m^2/g for CZSm to 22.9 and 22.3 m^2/g, respectively. The sample containing 3.0 wt% Ru witnessed a 57% increase in surface area as compared to CZSm, showing nearly 26 m^2/g. The average pore diameter decreased with Ru content.

The results of structural and textural analyses indicate how Ru cations are likely partially in solid solution within the CZSm lattice, while the presence of free RuO_2 domains, not detectable with the employed XRD apparatus, cannot be excluded.

3.3. Catalysts reducibility

The H_2-TPR profiles of CZSm support and R_xCZSm catalysts are shown in Fig. 2 and the respective hydrogen consumption, expressed in mmol H_2/g, are given in Table 3. H_2-TPR profiles can be divided into three regions according to the temperature ranges: the α-region denotes hydrogen consumptions occurring up to 300 °C, the β-region those occurring from 300 °C to 600 °C and the γ-region comprises the reductions occurring at T > 600 °C [36]. The slow but ever-increasing consumption of hydrogen in the 200–600 °C range (α- and β-regions), in the reduction profile of CZSm support, should be ascribed to the formation of oxygen vacancies, see Equation (15). This is consistent with TGA results of Fig. S3 and with literature reports dealing in particular with the reducibility of systems containing similar perovskite structures, such as $BaZrO_3$ [55–57].

$$O_O + H_2 \rightarrow H_2O + V_O^{\cdot} + 2e^- \tag{15}$$

At T > 600 °C, the hydrogen consumption shows a low intense asymmetric peak in the γ-region, which starts at about 600 °C and reaches a maximum at 640 °C. As already observed in the TGA profiles of Fig. S3, the presence of this peak is most likely due to the decomposition of $CaCO_3$ carbonate impurities [58–60] forming CO_2, as indicated in Equation (14). This is also confirmed by the slight pressure increase observed in the outlet stream near the temperature maximum of the γ-peak, reported in Fig. S4.

The addition of ruthenium dramatically affected the H_2-TPR profile. The sharp, intense peaks due to ruthenium reduction were observed at low-temperatures, between 100 and 350 °C (α-region), and at intermediate temperatures, between 350 and 550 °C (β-region). The first, sharp peak occurs in the α-region around 150 °C for R0.5CZSm and R1.5CZSm, respectively, while for R3.0CZSm the peak was observed at a slightly higher temperature (180 °C). Since this feature is particularly narrow and the intensity is proportional to the amount of Ru present in the sample, it is plausible that the associated hydrogen consumption is related to the superficial reduction of oxidized ruthenium domains and initial formation of Ru^0 aggregates that trigger the release of atomic hydrogen and favor the rapid reduction of surrounding species, as also pointed out by Madhavaram H. et al. [61]. The shift at higher temperatures observed for R3.0CZSm is coherent as larger RuO_2 particles expose less surface to the reducing agent, slightly increasing the activation energy of the reduction. A further consumption of hydrogen between 200 °C and 300 °C was observed, hardly visible in the case of R0.5CZSm but well resolved, with a maximum at 232 °C for R1.5CZSm. In R3.0CZSm, such feature was more intense, with a maximum at 238 °C followed by a shoulder at about 320 °C. A plausible interpretation is that these contributions in the 200–350 °C interval originate from Ru^{4+} species in solid solution with the perovskite lattice. As expected, the intensity of such features increased with Ru content.

The peaks in the β-range are only present in RxCZSm samples and are probably due to the production of methane owing to the partial conversion of carbonate impurities, as indicated in Equations (16) and (17). Carbonate impurities that are in closer contact with the Ru^0 particles formed in the α-region, can be easily hydrogenated through a Ru-hydrogen spill-over effect. This hypothesis is consistent with several experimental results where direct methanation of $CaCO_3$ was catalysed by metals such as Ni or Ru [62,63].

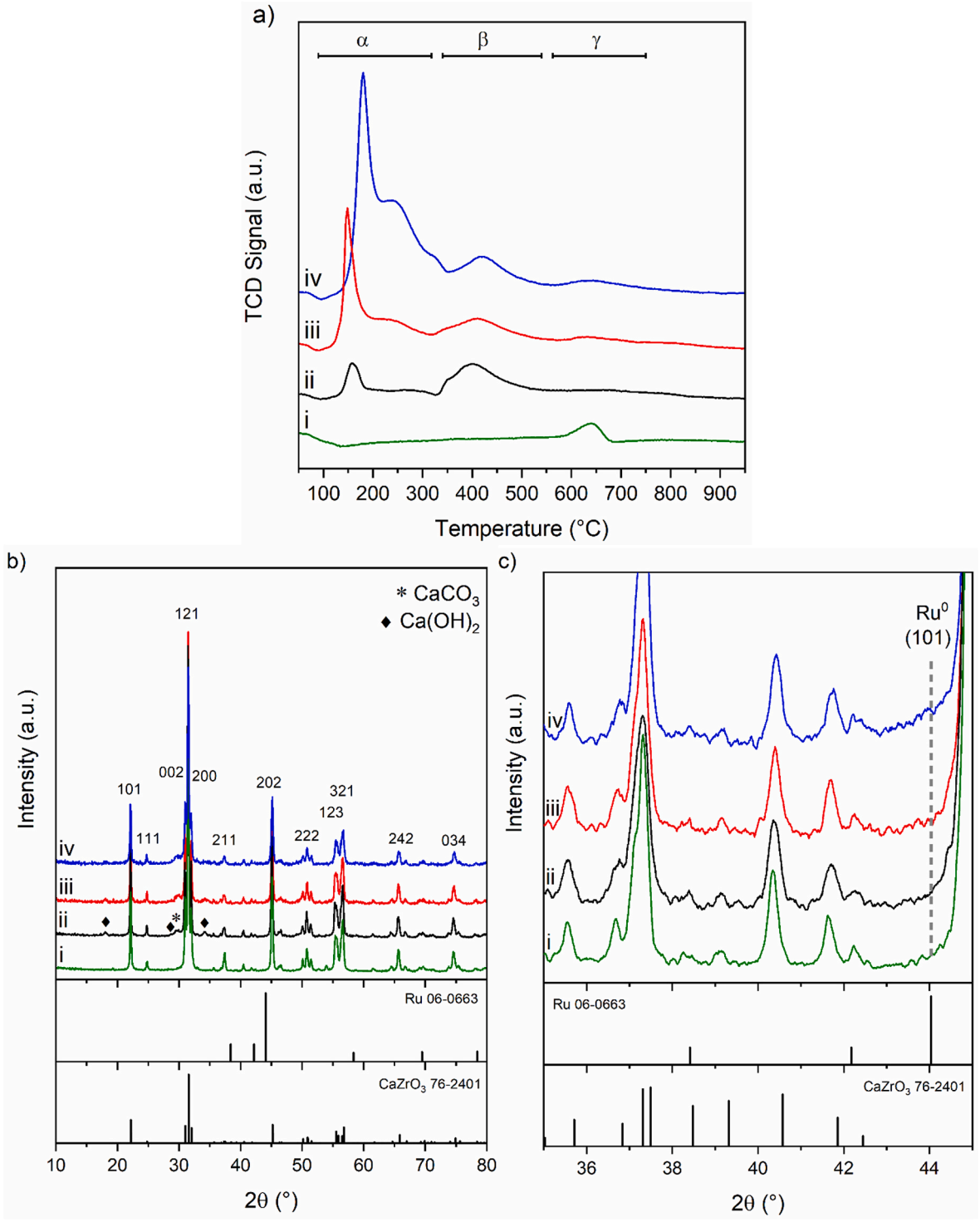

Fig. 2. – a) H_2-TPR profiles of the CZSm perovskite support (i), and Ru-containing catalysts: R0.5CZSm (ii), R1.5CZSm (iii) and R3.0CZSm (iv); b) XRD pattern of samples after 10 h reduction at 850 °C in 5% H_2/Ar: CZSm (i), R0.5CZSm (ii), R1.5CZSm (iii) and R3.0CZSm (iv). The PDF cards of $CaZrO_3$ and Ru were added as references; c) $35° < 2\theta < 45°$ magnification of b highlighting Ru^0 (101) peak position.

$$CaCO_3 + 4H_2 \rightarrow Ca(OH)_2 + CH_4 + H_2O \quad \Delta H^0 = -95.7\ kJ/mol \qquad (16)$$

$$CaCO_3 + 4H_2 \rightarrow CaO + CH_4 + 2H_2O \quad \Delta H^0 = 13.4\ kJ/mol \qquad (17)$$

In the γ region, the bulk decomposition of $CaCO_3$ observed for CZSm occurred and, as reported in Table 3, the TCD registered a higher signal, indicating a larger amount of decomposed $CaCO_3$. In fact, the partial Ru introduction into the crystal structure further destabilized the perovskite oxide support leading to a minor increase in carbonate impurities (minor increase in H_2 consumption): the corresponding pressure change in the gas outlet stream was registered for RxCZSm samples as well (Fig. S4). Finally, according to the previous discussion of the processes occurring in the β- and γ-regions, clearly only the area under the peaks belonging to the α-region corresponds to an effective consumption of hydrogen due to Ru^{4+}/Ru^0 reduction and the amount of consumed H_2 (Table 3) is proportional to the nominal Ru content. The larger reducibility observed

Table 3
The consumption of hydrogen in the α-, β- and γ-regions obtained from H_2-TPR profiles observed in Fig. 2a after baseline correction. Theoretical consumption and reducibility have been added for α-peaks considering the following reaction: $RuO_2 + 2H_2 \rightarrow Ru + 2H_2O$. * In the β- and y-peaks the TCD signal does not correspond only to the hydrogen consumption but also to the possible formation of CH_4 and the thermal decomposition of $CaCO_3$, respectively.

Sample	H_2 consumption (mmol/g)					
	α	H_2 theoretical cons. in α-region (mmol/g)	Reducibility (%)	β*	γ*	Total
CZSm					0.032	0.032
R0.5CZSm	0.102	0.105	97	0.163	0.073	0.338
R1.5CZSm	0.301	0.301	100	0.192	0.086	0.580
R3.0CZSm	0.713	0.59	121	0.195	0.084	0.992

Table 4
– Structural parameters obtained for reduced samples: CZSm, R0.5CZSm, R1.5CZSm, and R3.0CZSm.

Sample	Lattice parameters				Size–Strain Plot		
	a (Å)	b (Å)	c (Å)	Volume ($Å^3$)	D (nm)	ε^{S-S} (× 10^{-3})	R^2
CZSm	5.596	8.026	5.760	258.69	51.9	12.48	0.969
R0.5CZSm	5.599	8.035	5.770	259.62	80.1	12.90	0.932
R1.5CZSm	5.596	8.030	5.765	259.09	75.4	14.10	0.886
R3.0CZSm	5.599	8.024	5.761	258.84	54.5	15.42	0.927

for R3.0CZSm might be attributed to a larger overlap between α- and β-regions or to the presence of Ru oxidized states other than RuO_2.

Fig. 2b shows X-ray diffraction patterns of *x* wt.% Ru - $CaZr_{0.85}Sm_{0.15}O_{3-\delta}$ reduced samples. Structural parameters are listed in Table 4. The main orthorombic zirconate phase observed in the as prepared samples was mainly preserved, denoting remarkable redox stability of the oxide support. Nevertheless, in Ru-containing samples a larger presence of secondary phases was observed, most likely due to structural rearrangement after the oxide reduction process. The secondary phases due to Ca segregation during reduction are mainly identified as $Ca(OH)_2$ (PDF 01–1079), with minor traces of $CaCO_3$.

On one hand, as expected, the prolonged exposure to a highly reducing environment at operational temperature (850 °C) enlarged the crystallite size (D) as compared to the as prepared compounds (Table 4), yet on the other hand it increased the inhomogeneous strain (ε^{S-S}). The strain displayed an increasing trend, scaling with the amount of ruthenium, further supporting the hypothesis of Ru cations lattice inclusion.

Fig. 2c reports a magnification of the reduced RxCZSm diffraction patterns in the 35°–45° 2θ region: the presence of metallic ruthenium can only be observed for the R3.0CZSm sample, as the presence of a broad signal at 2θ = 44.04°, belonging to (101) Ru peak, is clearly observed, especially when R3.0CZSm XRD pattern is compared to those of the other reduced samples (detail reported in Fig. S5).

The morphologies of the CZSm and RxCZSm samples (x = 0.5, 1.5 and 3.0 wt %) after reduction are reported in Fig. 3. Fig. 3a shows the Ru-free catalyst support: CZSm appears made up of interconnected grains with a sponge-like surface on which irregularly shaped cavities are randomly distributed. This peculiar aspect is likely due to the gas release in the combustion step that occurred during the catalyst synthesis, and the same morphology is observed also for the oxide support in Ru-containing samples. Fig. 3b reveals the presence of few round nanoparticles with average diameter of 4.4 ± 0.9 nm, anchored on the surface of R0.5CZSm. As observed in Fig. 3c and 3d for R1.5CZSm (d = 5.1 ± 1.3 nm) and R3.0CZSm (d = 6.9 ± 1.5 nm), respectively, the NPs appear to increase in number and size together with the Ru content in the samples (size distributions for each sample are reported in Fig. S6). This result is coherent with the trend reported in H_2-TPR profiles of Fig. 2a and it is likely that the observed NPs consist of metallic Ru. In the R3.0CZSm sample it is possible to see how the Ru nanoparticles are distributed throughout the entire surface of CZSm, uniformly covering the oxide support. Such structure, ideal for a highly performing and long-lasting DRM catalytic system, has been obtained thanks to the direct addition of the Ru nitrate precursor in the solution combustion synthesis reactor. Since the previous characterizations supported the idea of a partial inclusion of Ru cations into the $CaZr_{0.85}Sm_{0.15}O_3$ lattice, ruthenium NPs exsolution upon the reduction treatment cannot be excluded. This phenomenon commonly occurred for perovskite oxides

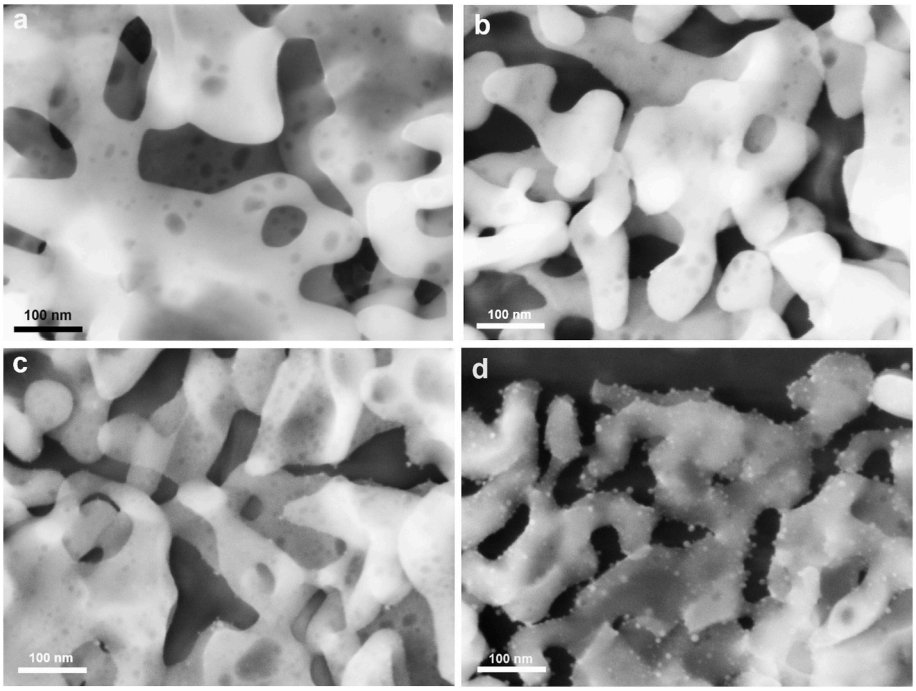

Fig. 3. FE-SEM images of the catalysts after 10 h reduction at 850 °C: a) CZS, b) R0.5CZSm, c) R1.5CZSm and d) R3.0CZSm.

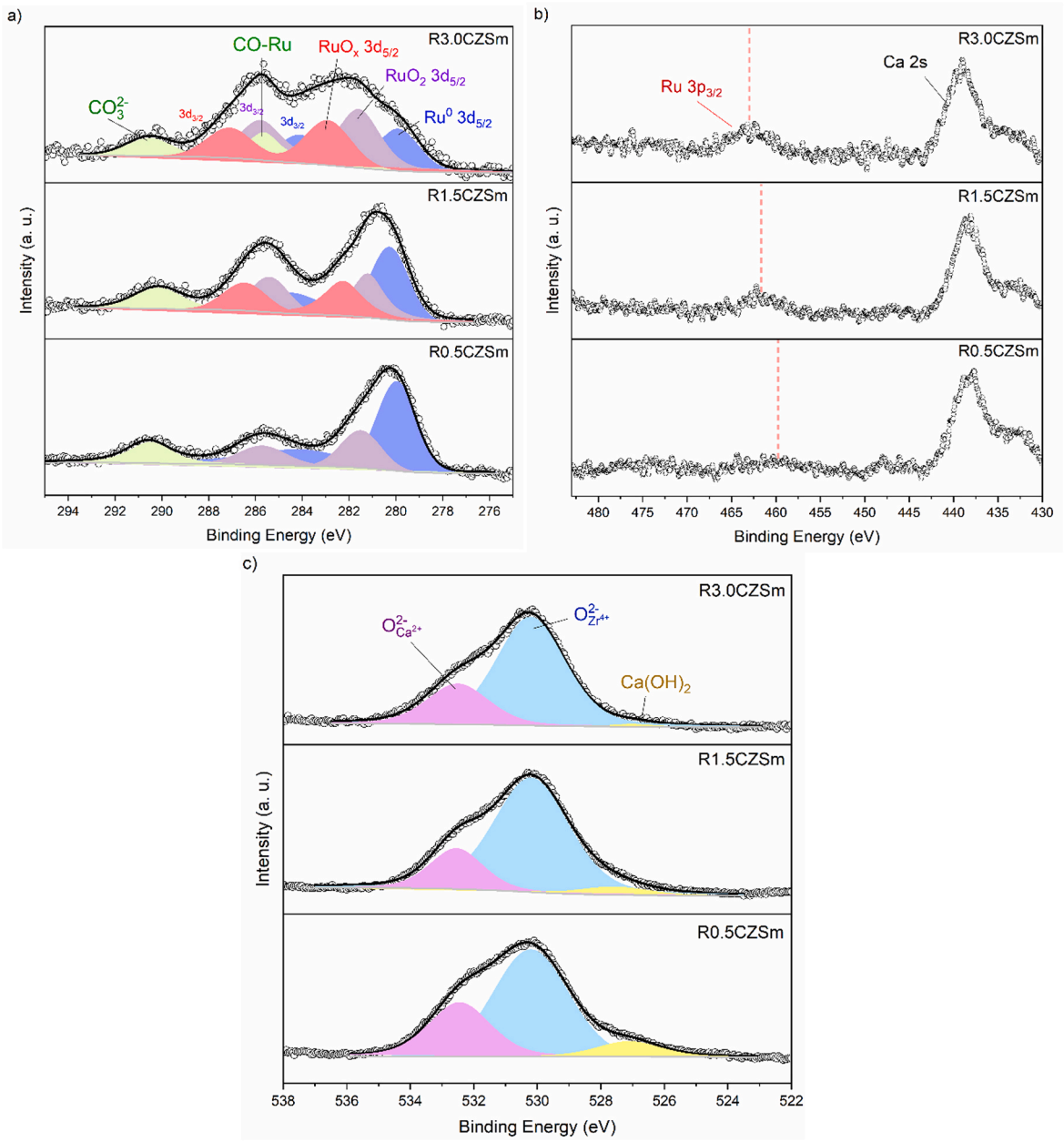

Fig. 4. XPS spectra of Ru 3d and C 1s region (a), of Ru $3p_{3/2}$ and Ca 2s (b), and of O 1s (c), for reduced RxCZSm samples.

Table 5
– Elemental abundance of the elements Ru, Sm, Ca and Zr on the surface of the reduced catalysts.

Sample	Ru %wt.	Sm %wt.	Ca %wt.	Zr %wt.
Nominal CZSm	–	12	21	41
R0.5CZSm	0.7	15.8	43.6	22.8
R1.5CZSm	1.8	14.7	41.8	21.7
R3.0CZSm	3.1	12.3	39.9	22.9

with limited amounts of noble metals included in the stoichiometry [24,64,65]. Thus, the presence of $Ca(OH)_2$ and $CaCO_3$ upon reduction in RxCZSm samples is likely ascribable to a structural rearrangement after metallic ruthenium exsolution. Indeed, the structural stress caused by Ru NPs growth and the produced rearrangement explain the observed progressive increase with Ru content of the inhomogeneous strain $\varepsilon^{S\text{-}S}$ reported in Table 4.

3.4. XPS analysis

XPS analyses of the reduced samples are reported in Fig. 4. The photoelectron peaks of Ru 3d, overlapped with the signal arising from C 1s, are shown in Fig. 4a, the peaks of Ru $3p_{3/2}$ and Ca 2s are displayed in Fig. 4b, while O 1s spectra are reported in Fig. 4c. Full survey spectra together with Ca 2p, Zr 3d and Sm 3d details are also reported in Fig. S7. A semi-quantitative analysis of the different species is reported in Table 5 for ruthenium, samarium, calcium and zirconium. Despite XRD patterns of Fig. 2b revealed how CZSm perovskite is the prevailing phase in the bulk of the samples, a larger amount of calcium was revealed on the surface via XPS analysis: this was expected due to the observed calcium hydroxide and carbonate superficial segregation after reduction.

Ru $3d_{5/2}$ signal is usually deconvoluted in three major components [66–68], with the respective $3d_{3/2}$ peak at constant 4.2 eV separation. The feature around 280 eV arises from metallic Ru, while the two components at higher binding energies belong to oxidized Ru states: one

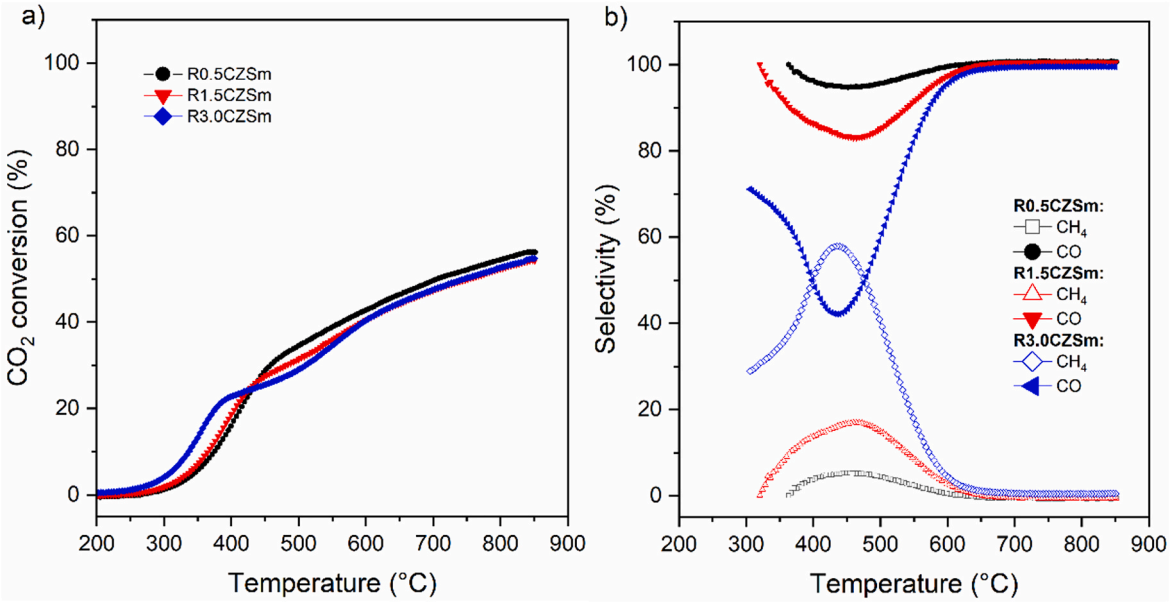

Fig. 5. CO_2 conversions (a), CH_4 and CO selectivities (b) for RWGS reaction. The activity was monitored with a temperature programmed reaction (3 °C/min) from 200 to 850 °C.

at ~281.2 eV and another at ~282.5 eV. The nature of the former is usually related to Ru^{4+} states in RuO_2, while the latter peak is associated to $Ru^{\delta+}$ cations, likely included in the oxide lattice: it was reported to result from different RuO_x components and spans broadly from 281.55 to 283.1 eV [67]. Wang et al. recorded XPS spectra of $LaFe_{0.9}Ru_{0.1}O_3$ during progressive reduction and Ru exsolution [66], observing how for the oxidized compound the prevailing ruthenium state was RuO_x, while the contribution at ~281.2 eV progressively appeared with increasing reduction, together with the Ru^0 peak. Here we believe that this latter contribution is related to RuO_2 formed on the Ru NPs surface after air exposure. The three components are clearly visible in R3.0CZSm, in which Ru^0 and RuO_2 signals arise respectively from the inner core and the outer shell of nanoparticles observed in Fig. 3d, while a significant amount of RuO_x is present in the oxide lattice. This latter contribution diminishes in R1.5CZSm and it is not revealed in R0.5CZSm, in which most of the ruthenium is exsolved at the surface. A low intense and broad C 1s contribution around 290.5 eV is present in all three spectra and it is related to surface carbonates ($CaCO_3$) species, while a further C 1s contribution is observed only in R3.0CZSm species at 285.7 eV. This feature is likely associated to carbonyl groups adsorbed on Ru NPs [69] and its higher intensity in R3.0CZSm is ascribable to the larger oxide surface coverage with Ru NPs.

The Ru $3p_{3/2}$ peak in the range between 450 eV and 470 eV is shown in Fig. 4b together with the signal arising from Ca 2s, that serves as a reference. Increasing the amount of ruthenium, the Ru $3p_{3/2}$ peak increases in intensity and shifts towards higher B.E. This indicates how the presence of oxidized Ru increases with Ru content [24,70].

The position and shape of the O 1s signal (Fig. 4c) is similar to that of $CaZrO_3$ samples obtained via similar synthetic routes [71] and can be deconvoluted into two main binding energy contributions at 529.5 and 531.8 eV. Here, a minor feature around 527.5 eV is also observable.

The former ones derive respectively from lattice O^{2-} bonded to Ca^{2+} and Zr^{4+} cations, respectively: it has been observed that when Zr^{4+} ions are doped into the CaO lattice the O 1s peak progressively shifts to lower binding energy [72]. The latter, lower intensity contribution at 527.5 eV, denotes the presence of superficial $Ca(OH)_2$ [73] and it is less intense in R3.0CZSm. The results of Ru 3d and O 1s spectra reveal how, increasing Ru content, Ru cations are partly retained within the perovskite lattice even after the reduction treatment. In fact, the XRD comparison of the most intense peak of all oxidized and reduced compounds provided in Fig. S8 shows how R3.0CZSm pattern retains a shift towards higher 2θ values after reduction. This likely limits the formation of Ca-based secondary phases.

In the Ca 2p spectra region (Fig. S7d), the prominent peak at 346.2 eV along with a satellite at 350 eV corresponds to the photoelectron emission from the $Ca2p_{3/2}$ and $Ca2p_{1/2}$ states. These peaks are characteristics of Ca^{2+} ions in oxides environment [72]. In the same region also the Zr $3p_{3/2}$ feature can be detected at 332 eV and the Zr $3p_{1/2}$ at 343 eV, overlapped with the calcium $3p_{3/2}$ emission. Fig. S7e shows Zr $3d_{3/2}$ and $3d_{5/2}$ overlapped peaks. Finally, in Fig. S7f the results for Sm 3d region are reported, where it is possible to see the doublet at 1083 eV and at 1110 eV relative to the samarium oxide inserted in the structure. No significant differences can be found in the Ca, Zr and Sm XPS spectra of RxCZSm samples.

3.5. Reverse water gas shift activity

Assessing the activity for RWGS allows to evaluate the catalysts behavior towards the main competitive reaction to DRM. The RxCZSm were thus tested in a mixture containing H_2:CO_2:N_2, using a volumetric ratio of 20:20:60.

Fig. 5 illustrates the trend of CO_2 conversion and selectivity to CH_4 and CO for the RWGS reaction as a function of temperature. The conversions showed a rapid initial growth at temperature < 500 °C, which levelled off and then gradually increased again, almost reaching the thermodynamic value, 55% CO_2 at 850 °C. Initially, the conversion was low up to 300 °C then it was triggered, as ruthenium started to be reduced to Ru^0: an increase between 300 °C and 400 °C was observed and conversion values increased according to Ru content. In the region between 400 °C and 600 °C the CO_2 conversion scaled inversely with Ru content. This effect was due to the occurrence of the concomitant methanation reaction, that is favored in this temperature range, although the H_2/CO_2 ratio is far from the stoichiometric value. The performance towards methanation of Ru-supported systems was recently shown to be highly dependent on Ru content, with the highest activity observed for 2.5 wt% Ru on ceria [74]. However, RWGS returned to be favored for T > 600 °C, and no significant difference was observed in the conversion, which remained essentially the same up to 850 °C for all catalysts.

The selectivity for CH_4 and CO reported in Fig. 5b confirmed the

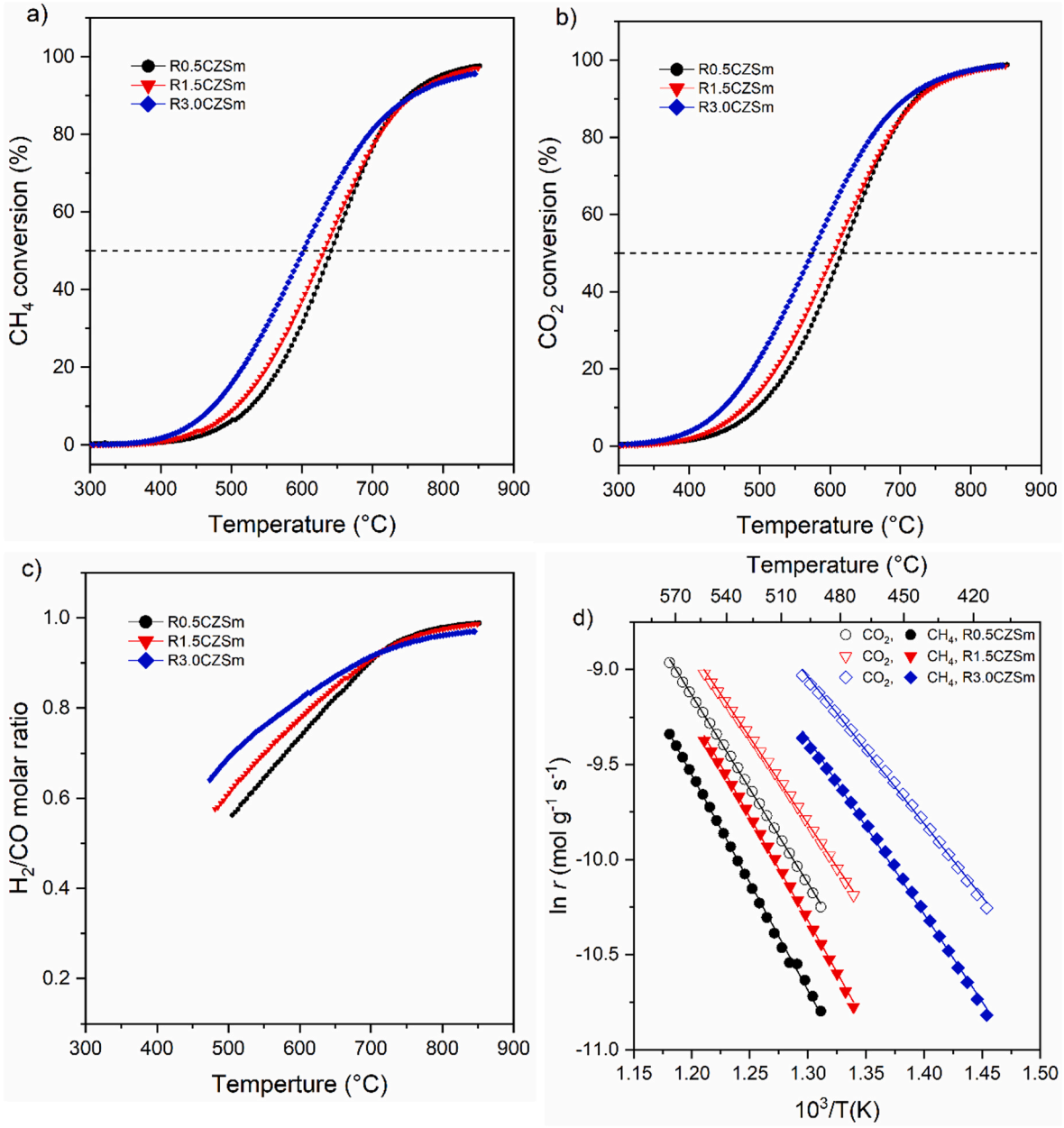

Fig. 6. CO_2 (a) and CH_4 (b) conversions and H_2/CO molar ratio (c) for DRM reaction from 300 to 850 °C with (4 °C/min). Arrhenius diagram of reaction rate for CO_2 (open symbols) and CH_4 (closed symbols) (d).

RxCZSm activity towards methanation. Below 600 °C a maximum was observed for the formation of CH_4 (corresponding to a minimum for CO formation), which was clearly proportional to the Ru content: i.e., relatively to CH_4, 58% at 438 °C for R3.0CZSm, 17% at 463 °C for R1.5CZSm and 5% at about 463 °C for R0.5CZSm. Basically, the Ru content at lower temperatures promoted the formation of methane with a 1:1 H_2/CO_2 ratio. However, above 650 °C there was no significant difference with Ru content, as the conversion and selectivity to CO showed the same trend for all catalysts tested.

For T > 600 °C, when DRM reaction is favored, methanation activity is negligible while RWGS activity resulted in the same CO_2 conversions (55%) and selectivity towards CO for all the tested catalysts, independently from Ru content.

3.6. DRM activity

Fig. 6 shows the temperature-programmed DRM reaction results, showing the CH_4 and CO_2 conversions, the corresponding H_2/CO ratio, and the Arrhenius plot of the reaction rates.

For all samples, the conversion curves showed a sigmoidal trend that flattened at temperatures above 750 °C, reaching about 98% conversion for both reactants CH_4 and CO_2 at 850 °C. The increase in Ru content progressively lowered the temperature at which a 50% CH_4 conversion was achieved: 640, 631, and 602 °C for R0.5CZSm, R1.5CZSm, and R3.0CZSm, respectively. This positive effect was found also in the case of CO_2 conversion, which showed 50% conversion at 615, 604, and 574 °C for R0.5CZSm, R1.5CZSm, and R3.0CZSm, respectively. The higher conversion of CO_2 at each temperature is due to the simultaneous RWGS reaction.

The H_2/CO ratio, plotted versus temperature in Fig. 6c, increased with temperature, and at 550 °C reached values of 0.64, 0.70 and 0.76 for Ru0.5CZSm, Ru1.5CZSm, and R3.0CZSm, respectively. The ratio then levelled off to about 0.98 at the maximum temperature of 850 °C, independently on the amount of Ru. It is possible to see how the effect of

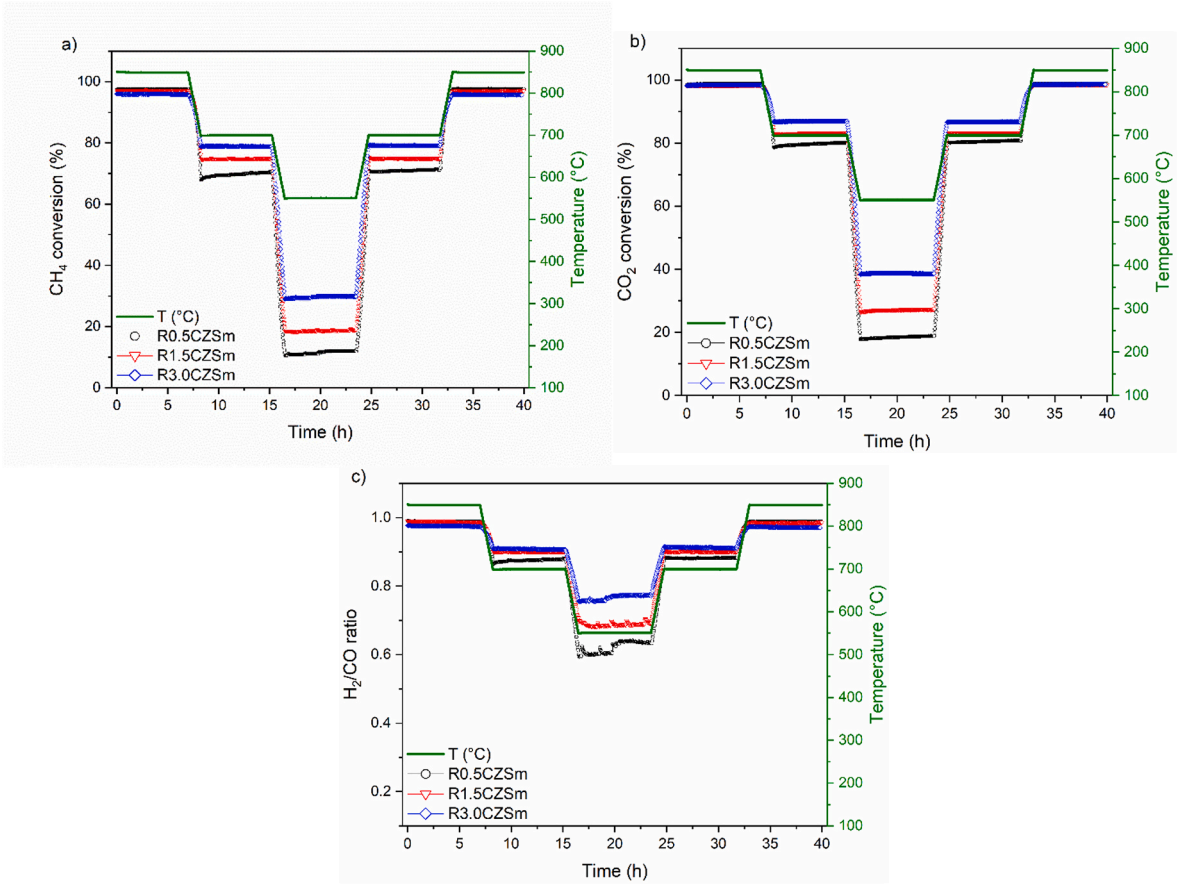

Fig. 7. Time-on-stream reaction at 550, 700, and 850 °C with temperature changes of 3 °C/min and each isothermal step of 5 h for RxCZSm samples: CH_4 (a) and CO_2 (b) conversions and H_2/CO molar ratio (c).

temperature changed the selectivity of the overall reaction. At lower temperature the three catalysts exhibited a decreasing selectivity in function of the ruthenium content. Furthermore, above 750 °C no differences in conversion can be observed for the three cases, confirming that in these conditions the effect of RWGS was independent on the Ru loading. The apparent activation energy for the reagents was calculated from the Arrhenius plot of Fig. 6d and values are reported in Table S2. Linear fits of reaction rates data in all cases showed an R^2 greater than 0.9. The apparent activation energy decreased proportionally to the increase in Ru content: from 94.1 to 76.5 kJ mol^{-1} for the CH_4 consumption rate in R0.5CZSm and R3.0CZSm, respectively, and from 82.1 to 64.1 kJ mol^{-1} for CO_2 consumption rate in R0.5CZSm and R3.0CZSm, respectively. The higher activation energy for CH_4 indicates that, in the considered temperature range, the rate-determining step is the activation of CH_4 at Ru sites to form H*- and C*-active species. However, the contribution to overall CO_2 conversion due to the RWGS parallel reaction must be considered.

As previously reported in literature [75–77], the use of supports with moderate oxygen mobility enhances the metal-support interaction and possibly the rate of conversion of methane. Here CH_4 is activated on metallic Ru sites while CO_2 activation is also promoted by the surface oxygen vacancies of CZSm support.

3.7. Time-on-stream (ToS) durability tests and spent catalysts characterization

The catalysts stability was tested monitoring the CH_4 conversion, the CO_2 conversion and the H_2/CO ratio over time, and results are reported in Fig. 7a, 7b and 7c, respectively. To assess the catalysts durability and tolerance to carbon formation, the temperature was also varied during the test: first from 850 °C to 700 °C and to 550 °C, then up again to 700 °C and to 850 °C. Overall the stability tests consisted of a total duration of over 65 h, considering the initial heating ramp and final cooling ramp (1 °C/min) performed in the DRM feed composition, not shown in Fig. 7. At the initial isothermal conditions of 850 °C, the reactant turnovers were stable and very similar for the three systems. The dependence on Ru content was minimal, although CH_4 conversion scaled inversely with respect to Ru amount. Likely, the presence of few, highly distributed Ru nanoparticles in R0.5CZSm represented the optimal loading to favor metal-support interaction at 850 °C resulting in a constant 2% higher methane conversion as compared to R3.0CZSm observed both in the first and the last 850 °C steps. Decreasing the temperature down to 700 °C, R3.0CZSm sample showed high and constant conversion, R1.5CZSm had lower activity, yet still constant, while R0.5CZSm showed the lowest performance and a slower activation, reaching stability only in the final part of the isothermal segment. This trend was even more evident at 550 °C, where the catalytic activity was observed to be highly dependent on Ru content. Oscillations are clearly visible at 550 °C in the H_2/CO trend of Fig. 7c, which are directly related only to CH_4 conversion (Fig. 7a), not revealed in CO_2 conversion (Fig. 7b), and decreased in magnitude with Ru content. While at higher temperature CH_4 undergoes direct dissociation on a metal surface, the activation is believed to occur via intermediate formations at 550 °C [17]. Recently, the presence of oxidized ruthenium ($Ru^{\delta+}$) in Ru-supported systems has been proven to be pivotal in favoring methane activation at 500 °C, while oxygen vacancies in the support lattice contribute to directly activate CO_2 [78]. Here, Ru XPS spectra of Fig. 4a and 4b revealed a remarkably larger RuO_x/Ru^0 ratio for R3.0CZSm. Moreover, according to Fig. 5a RWGS scaled inversely with Ru content at 550 °C: as a result, CO_2 conversion was 58% larger than CH_4

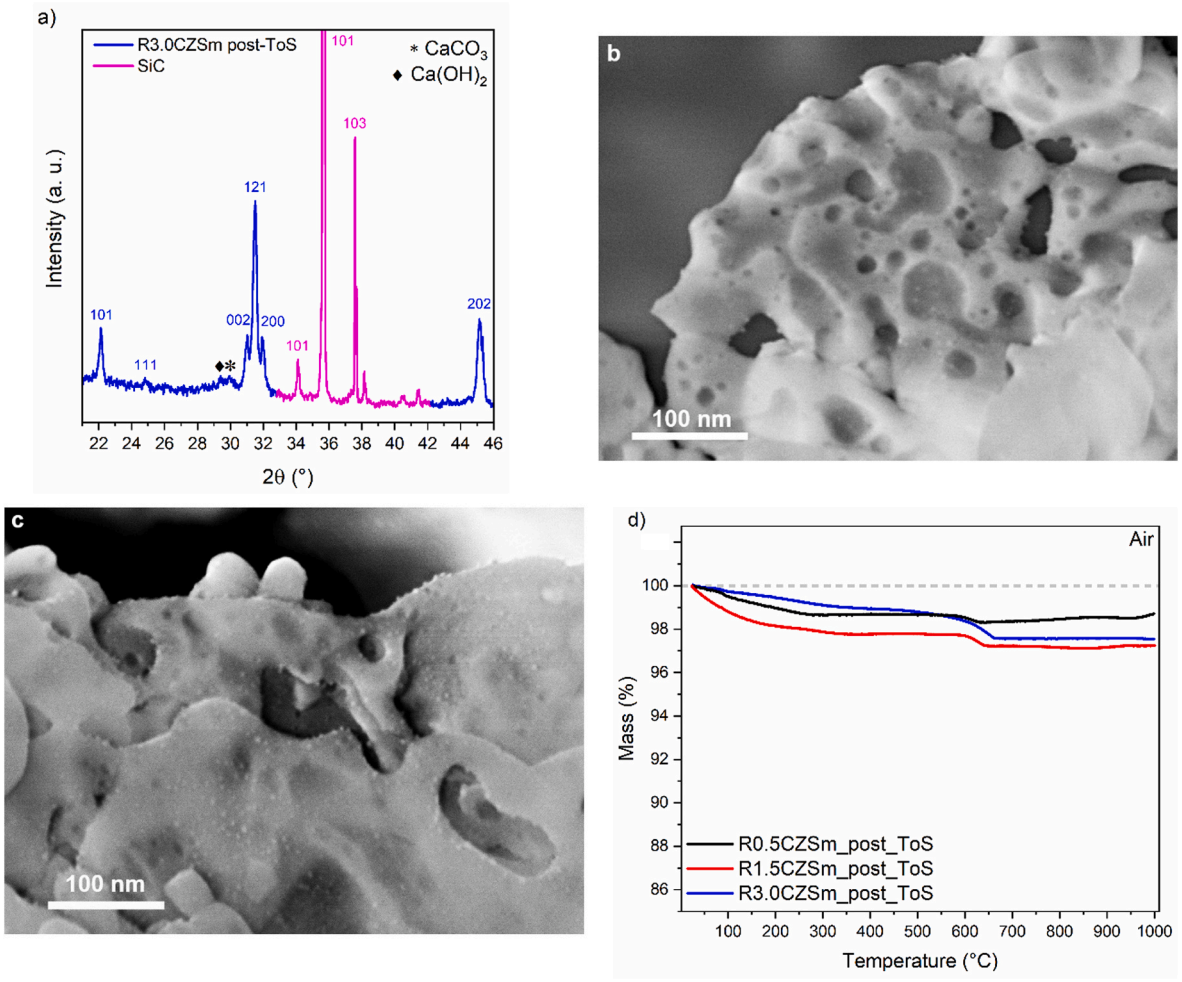

Fig. 8. a) XRD pattern in the 21°–46° 2θ range of R3.0CZSm sample after ToS test reported in Fig. 7. The sharp peaks between 33° and 42° belong to residual SiC fragments, remained after sieving the spent catalyst powders; representative FE-SEM images of R1.5CZSm (b) and R3.0CZSm (c) samples after ToS test; (d) Thermogravimetric analyses results of spent RxCZSm samples after ToS test.

conversion for R0.5CZSm while only 30% larger for R3.0CZSm. Overall, while fewer Ru sites are optimal to promote DRM at 850 °C, a larger coverage of the CZSm support with ruthenium in a partially oxidized state promoted adsorption and activation of methane, limiting at the same time RWGS at 550 °C. In Table S3 the performance of R3.0CZSm is compared to recently published Ru-containing DRM catalysts [28,31,79].

Fig. 8a reports the XRD pattern of R3.0CZSm after the stability test. Despite the intense and sharp peaks ascribable to SiC residues in the 2θ = 34°–44° region, the characteristic peaks of R3.0CZSm structure are clearly visible, showing that the catalyst structure was preserved after ToS. Fig. 8b and 8c report the FE-SEM morphology of the spent catalysts. No significant sintering of the oxide support grains is visible. No visible signs of sintering or coarsening of the surface Ru nanoparticles were revealed: these appear homogeneously distributed and well-anchored to the substrate both for R1.5CZSm and for R3.0CZSm. Their average diameter, 4.1 ± 0.8 nm for R1.5CZSm and 4.6 ± 0.8 nm for R3.0CZSm is smaller if compared to those reported in Fig. 3c and 3d (size distributions for each sample are reported in Fig. S9). This can be attributed to the exposure to different reducing environments: 10 h in 5%H_2/Ar for RxCZSm samples reported in Fig. 3 and over 65 h in DRM mixture for samples reported in Fig. 8. No readily identifiable carbon deposition could be detected and, to provide a more reliable evidence, the spent catalyst powder was collected, sieved and subjected to a thermogravimetric analysis in air to favor the combustion of any carbonaceous formation. TGA results are reported in Fig. 8d: the total mass loss up to 1000 °C remained below 3 wt% and it was equally distributed between desorption of adsorbed species at T < 250 °C and decomposition of calcium carbonates in the 600–650 °C, which are typically observed on calcium zirconates, as stated in section 3.1. No evidence of mass loss due to the combustion of carbon-based material was observed.

4. Conclusions

Three different ruthenium loadings (0.5, 1.5 and 3.0 wt%) on a B-site Sm-substituted calcium zirconate perovskite oxide support Ru *x* wt.% - $CaZr_{0.85}Sm_{0.15}O_{3-\delta}$ (CZSm) were tested as catalysts for dry reforming of methane. A calcium zirconate substrate was chosen for its high redox stability and surface basicity. 15 mol% samarium doping greatly increased the extent of perovskite lattice oxygen vacancies. The adopted glycine solution combustion synthesis method endowed the system with high surface area, reaching 25.98 ± 0.07 m^2/g for R3.0CZSm. The ruthenium precursor was directly added in the initial nitrates solution and largely affected the obtained perovskite oxide structural and textural properties. After exposure to reducing conditions, Ru nanoparticles (d < 10 nm) were revealed on the oxide surface, whose extent and substrate surface coverage depended on Ru content: from few and isolated NPs for R0.5CZSm to a homogeneous surface distribution for R3.0CZSm. XPS analysis on the reduced samples revealed the simultaneous presence of metallic and oxidized Ru states, the latter increased with Ru content. The catalysts were first tested for RWGS reaction: the presence of Ru favored CO_2 conversion at lower temperatures (T <

300 °C), yet a net decrease was observed between 400 °C and 600 °C due to the concomitant methanation reaction, favored by a larger presence of ruthenium. RWGS activity reached 55% CO_2 conversion at 850 °C, independently on the Ru content. R0.5CZSm catalyst showed highest activity towards DRM reaction at 850 °C, which, on the other hand, was proportional to the amount of supported ruthenium for T < 700 °C. In fact, R3.0CZSm displayed a 50% CH_4 conversion at 602 °C, a H_2/CO ratio of 0.77 at 550 °C and apparent activation energies of 76.5 kJ mol^{-1} and 64.1 kJ mol^{-1} for CH_4 and CO_2, respectively. The catalytic behavior vs time-on-stream was monitored at 850 °C, 700 °C and 550 °C for over 40 h. All the three systems revealed remarkable stability over time without losing performance or deactivating. The catalyst with the lowest amount of ruthenium (0.5 wt%) displayed the highest CH_4 conversion, 97.6% at 850 °C, while the one with the highest loading, R3.0CZSm, outperformed the others at 550 °C. Post ToS analyses on spent catalysts revealed structural integrity and the complete absence of formed carbon species.

CRediT authorship contribution statement

Leonardo Duranti: Writing – review & editing, Writing – original draft, Investigation, Formal analysis, Data curation. **Umberto Pasqual Laverdura:** Writing – review & editing, Writing – original draft, Investigation, Formal analysis, Data curation, Conceptualization. **Elisabetta Di Bartolomeo:** Writing – review & editing, Supervision, Project administration, Funding acquisition. **Maria Luisa Grilli:** Writing – review & editing, Supervision, Project administration, Funding acquisition, Formal analysis. **Rosa Chierchia:** Investigation, Formal analysis. **Claudio Larosa:** Formal analysis. **Alessio Varotto:** Investigation, Formal analysis. **Simonetta Tuti:** Writing – review & editing. **Silvia Licoccia:** Writing – review & editing, Resources, Funding acquisition. **Igor Luisetto:** Writing – review & editing, Visualization, Validation, Methodology, Investigation, Funding acquisition, Formal analysis, Data curation, Conceptualization.

Data availability

Data will be made available on request.

Declaration of competing interest

The authors declare that they have no known competing financial interests or personal relationships that could have appeared to influence the work reported in this paper.

Acknowledgments

This manuscript is *in memoriam* of Dr. Igor Luisetto, who first designed and imagined this work. The authors are heartfully grateful to him for his attitude, rigorous scientific method, teachings and profound, inspirational humanity.

This work was funded by the FSE-REACT EU Programma Operativo Nazionale Ricerca e Innovazione 2014–2020 (MUR) for the research contract "Towards the energy transition: multifunctional materials for solid oxide reversible cells" CUP E81B21004910005 and PRIN-2022 project – Prot.2022ZWYSKY "Advanced materials for reversible solid oxide cells (AMARILLO)" CUP E53D2300537 of the Italian Ministry for University and Research (MUR) funded by the European Union – Next Generation EU, and by the Italian Piano Nazionale di Ripresa e Resilienza PNRR Mission 4 IR0000020 – ECCSELLENT - Development of ECCSEL-R.I. ItaLian facilities: usEr access, services and loNg-Term sustainability.

Appendix A. Supplementary data

Supplementary data to this article can be found online at https://doi.org/10.1016/j.ijhydene.2025.01.366.

References

[1] Shtjefni D, Kuzov T, Clocchiatti A, Lecomte E, Lonning EVW, Baleva S, Tzimas E. SET PLAN Progress report 2021. 2021.
[2] Gangadharan P, Kanchi KC, Lou HH. Evaluation of the economic and environmental impact of combining dry reforming with steam reforming of methane. Chem Eng Res Des 2012;90:1956–68.
[3] Luisetto I, Mancini MR, Della Seta L, Chierchia R, Vanga G, Grilli ML, et al. CaO–CaZrO3 mixed oxides prepared by auto–combustion for high temperature CO2 capture: the effect of CaO content on cycle stability. Metals 2020;10:750.
[4] Venugopal M, Padma Kumar H, Satheesh R, Jayakrishnan R. Tailoring the photoluminescent properties of samarium and dysprosium codoped calcium zirconate perovskites for WLED applications. Int J Appl Ceram Technol 2019;16:1228–38.
[5] Lanzini A, Leone P, Guerra C, Smeacetto F, Brandon N, Santarelli M. Durability of anode supported Solid Oxides Fuel Cells (SOFC) under direct dry-reforming of methane. Chem Eng J 2013;220:254–63.
[6] Shiratori Y, Ijichi T, Oshima T, Sasaki K. Internal reforming SOFC running on biogas. International Journal of Hydrogen Energy 2010;35:7905–12.
[7] Sarno C, Luisetto I, Zurlo F, Licoccia S, Di Bartolomeo E. Lanthanum chromite based composite anodes for dry reforming of methane. International Journal of Hydrogen Energy 2018;43:14742–50.
[8] Aramouni NAK, Touma JG, Tarboush BA, Zeaiter J, Ahmad MN. Catalyst design for dry reforming of methane: analysis review. Renew Sustain Energy Rev 2018;82:2570–85.
[9] Wittich K, Krämer M, Bottke N, Schunk SA. Catalytic dry reforming of methane: insights from model systems. ChemCatChem 2020;12:2130–47.
[10] Arora S, Prasad R. An overview on dry reforming of methane: strategies to reduce carbonaceous deactivation of catalysts. RSC Adv 2016;6:108668–88.
[11] Nair MM, Kaliaguine S. Structured catalysts for dry reforming of methane. New J Chem 2016;40:4049–60.
[12] Luyben WL. Design and control of the dry methane reforming process. Ind Eng Chem Res 2014;53:14423–39.
[13] Onstot W, Minet R, Tsotsis T. Design aspects of membrane reactors for dry reforming of methane for the production of hydrogen. Ind Eng Chem Res 2001;40:242–51.
[14] Serrano-Lotina A, Daza L. Influence of the operating parameters over dry reforming of methane to syngas. Int J Hydrogen Energy 2014;39:4089–94.
[15] Varotto A, Pasqual Laverdura U, Feroci M, Grilli ML. Photo-thermal dry reforming of methane with PGM-free and PGM-based catalysts: a review. Materials 2024;17:3809.
[16] Awad MM, Hussain I, Mustapha U, Taialla OA, Alhassan AM, Kotob E, et al. A critical review of recent advancements in catalytic dry reforming of methane: physicochemical properties, current challenges, and informetric insights. Int J Hydrogen Energy 2024;76:202–33.
[17] Pakhare D, Spivey J. A review of dry (CO 2) reforming of methane over noble metal catalysts. Chem Soc Rev 2014;43:7813–37.
[18] Liang D, Wang Y, Wang Y, Chen M, Xie X, Li C, et al. Dry reforming of methane for syngas production over noble metals modified M-Ni@ S-1 catalysts (M= Pt, Pd, Ru, Au). Int J Hydrogen Energy 2024;51:1002–15.
[19] Shen X, Wang T, Sun S, Zhong X, Shi W, Song W, et al. Revealing the catalytic ability of 5% Rh–5% Pt–5% Al2O3–85% CeO2 for CH4-based mixing fuel gases operating at 550° C. Int J Hydrogen Energy 2024;74:128–35.
[20] Le Saché E, Reina T. Analysis of Dry Reforming as direct route for gas phase CO2 conversion. The past, the present and future of catalytic DRM technologies. Prog Energy Combust Sci 2022;89:100970.
[21] Zhang G, Liu J, Xu Y, Sun Y. A review of CH4CO2 reforming to synthesis gas over Ni-based catalysts in recent years (2010–2017). Int J Hydrogen Energy 2018;43:15030–54.
[22] Nagaoka K, Okamura M, Aika K-i. Titania supported ruthenium as a coking-resistant catalyst for high pressure dry reforming of methane. Catal Commun 2001;2:255–60.
[23] Zhang J-C, Ge B-H, Liu T-F, Yang Y-Z, Li B, Li W-Z. Robust ruthenium-saving catalyst for high-temperature carbon dioxide reforming of methane. ACS Catal 2019;10:783–91.
[24] Marasi M, Duranti L, Luisetto I, Fabbri E, Licoccia S, Di Bartolomeo E. Ru-doped lanthanum ferrite as a stable and versatile electrode for reversible symmetric solid oxide cells (r-SSOCs). J Power Sources 2023;555:232399.
[25] Gao X, Wang Z, Ashok J, Kawi S. A comprehensive review of anti-coking, anti-poisoning and anti-sintering catalysts for biomass tar reforming reaction. Chem Eng Sci X 2020;7:100065.
[26] Caillot T, Gauthier G, Delichère P, Cayron C, Aires FCS. Evidence of anti-coking behavior of La0. 8Sr0. 2Cr0. 98Ru0. 02O3 as potential anode material for Solid Oxide Fuel Cells directly fed under methane. J Catal 2012;290:158–64.
[27] Luisetto I, Sarno C, De Felicis D, Basoli F, Battocchio C, Tuti S, et al. Ni supported on γ-Al2O3 promoted by Ru for the dry reforming of methane in packed and monolithic reactors. Fuel Process Technol 2017;158:130–40.
[28] Kim GS, Lee BY, Ham HC, Han J, Nam SW, Moon J, et al. Highly active and stable Sr0. 92Y0. 08Ti1− xRuxO3− d in dry reforming for hydrogen production. Int J Hydrogen Energy 2019;44:202–12.
[29] Sun J, Yamaguchi D, Tang L, D'Angelo AM, Chiang K. Low temperature catalytic activity of hydrothermally synthesised ruthenium promoted ceria-zirconia

composites for reforming CO2-rich methane. Int J Hydrogen Energy 2024;51:822–36.
[30] Jun Y-B, Park J-H, Kim H-S, Jung K-S, Yoon S-P, Lee C-W. A simulation model for ruthenium-catalyzed dry reforming of methane (DRM) at different temperatures and gas compositions. Int J Hydrogen Energy 2024;49:786–97.
[31] Naeem MA, Abdala PM, Armutlulu A, Kim SM, Fedorov A, Müller CR. Exsolution of metallic Ru nanoparticles from defective, fluorite-type solid solutions Sm2Ru x Ce2–x O7 to impart stability on dry reforming catalysts. ACS Catal 2019;10:1923–37.
[32] Zhang J, Li M, Jin F, Zhang J, Li R, Li X, et al. Direct carbon dioxide-methane solid oxide fuel cells combined with in-situ exsolution perovskite La0. 75Sr0. 25Cr0. 5Fe0. 4Cu0. 1O3-δ-based dry reforming catalysts. Int J Hydrogen Energy 2024;55:572–80.
[33] Sažinas R, Sakaguchi I, Einarsrud M-A, Grande T. 96Zr tracer diffusion in AZrO3 (A= Ca, Sr, Ba). INORGA 2018;6:14.
[34] Vera CYR, Ding H, Peterson D, Gibbons WT, Zhou M, Ding D. A mini-review on proton conduction of BaZrO3-based perovskite electrolytes. J Phys: Energy 2021;3:032019.
[35] Zhang W, Hu YH. Progress in proton-conducting oxides as electrolytes for low-temperature solid oxide fuel cells: from materials to devices. Energy Sci Eng 2021;9:984–1011.
[36] Memon MA, Zhou W, Ajmal M, Jiang Y, Zhang C, Zhang J, et al. Ni–CaZrO3 with perovskite phase loaded on ZrO2 for CO2 methanation. Int J Hydrogen Energy 2024;92:1202–13.
[37] Giannici F, Shirpour M, Longo A, Martorana A, Merkle R, Maier J. Long-range and short-range structure of proton-conducting Y: BaZrO3. Chem Mater 2011;23:2994–3002.
[38] Ferreira A, Gharbage B, Labrincha J, Frade J. SrZrO 3-based proton conducting materials with La additions. Ionics 1995;1:474–81.
[39] Lyagaeva J, Danilov N, Korona D, Farlenkov A, Medvedev D, Demin A, et al. Improved ceramic and electrical properties of CaZrO3-based proton-conducting materials prepared by a new convenient combustion synthesis method. Ceram Int 2017;43:7184–92.
[40] Fop S. Solid oxide proton conductors beyond perovskites. J Mater Chem A 2021;9:18836–56.
[41] Di Bartolomeo E, D'Epifanio A, Pugnalini C, Giannici F, Longo A, Martorana A, et al. Structural analysis, phase stability and electrochemical characterization of Nb doped BaCe0. 9Y0. 1O3− x electrolyte for IT-SOFCs. J Power Sources 2012;199:201–6.
[42] Wu J, Gao J, Lian S, Li J, Sun K, Zhao S, et al. Engineering the oxygen vacancies enables Ni single-atom catalyst for stable and efficient CH activation. Appl Catal B Environ 2022;314:121516.
[43] De Florio DZ, Muccillo R, Esposito V, Di Bartolomeo E, Traversa E. Preparation and electrochemical characterization of perovskite/YSZ ceramic films. J Electrochem Soc 2004;152:A88.
[44] Luisetto I, Tuti S, Romano C, Boaro M, Di Bartolomeo E, Kesavan JK, et al. Dry reforming of methane over Ni supported on doped CeO2: new insight on the role of dopants for CO2 activation. J CO2 Util 2019;30:63–78.
[45] Goldwasser M, Rivas M, Pietri E, Pérez-Zurita MJ, Cubeiro ML, Gingembre L, et al. Perovskites as catalysts precursors: CO2 reforming of CH4 on Ln1− xCaxRu0. 8Ni0. 2O3 (Ln= La, Sm, Nd). Appl Catal A: Gen. 2003;255:45–57.
[46] Prioriello A, Duranti L, Luisetto I, Sanna F, Larosa C, Grilli ML, et al. Structured catalyst for indirect internal reforming (IIR) of biogas in solid oxide fuel cell (SOFC). Catalysts 2023;13:1129.
[47] Aguiar P, Chadwick D, Kershenbaum L. Modelling of an indirect internal reforming solid oxide fuel cell. Chem Eng Sci 2002;57:1665–77.
[48] Rashid NLRM, Samat AA, Jais AA, Somalu MR, Muchtar A, Baharuddin NA, et al. Review on zirconate-cerate-based electrolytes for proton-conducting solid oxide fuel cell. Ceram Int 2019;45:6605–15.
[49] Deganello F, Marcì G, Deganello G. Citrate–nitrate auto-combustion synthesis of perovskite-type nanopowders: a systematic approach. J Eur Ceram Soc 2009;29:439–50.
[50] Komova OV, Mukha SA, Ozerova AM, Odegova GV, Simagina VI, Bulavchenko OA, et al. The Formation of perovskite during the combustion of an energy-rich Glycine–nitrate precursor. Materials 2020;13:5091.
[51] Ianoş R, Barvinschi P. Solution combustion synthesis of calcium zirconate, CaZrO3, powders. J Solid State Chem 2010;183:491–6.
[52] Duranti L, Luisetto I, Licoccia S, Del Gaudio C, Di Bartolomeo E. Electrochemical performance and stability of LSFMn+ NiSDC anode in dry methane. Electrochim Acta 2020;362:137116.
[53] Luisetto I, Tuti S, Di Bartolomeo E. Co and Ni supported on CeO2 as selective bimetallic catalyst for dry reforming of methane. Int J Hydrogen Energy 2012;37:15992–9.
[54] Thommes M, Kaneko K, Neimark A, Olivier J, Rodriguez-Reinoso F, Rouquerol J. KS Sing Physisorption of gases, with special reference to the evaluation of surface area and pore size distribution. IUPAC Technical Report) 2016;87. https://doiorg/101515/ci-2016-0119.25.
[55] de Caprariis B, de Filippis P, Palma V, Petrullo A, Ricca A, Ruocco C, et al. Rh, Ru and Pt ternary perovskites type oxides BaZr (1-x) MexO3 for methane dry reforming. Appl Catal Gen 2016;517:47–55.
[56] Shirpour M, Merkle R, Maier J. Evidence for space charge effects in Y-doped BaZrO3 from reduction experiments. Solid State Ionics 2012;216:1–5.
[57] Wang Z, Liu B, Lin J. Highly effective perovskite-type BaZrO3 supported Ru catalyst for ammonia synthesis. Appl Catal Gen 2013;458:130–6.
[58] Li Z, Yang D-P, Chen Y, Du Z, Guo Y, Huang J, et al. Waste eggshells to valuable Co3O4/CaCO3 materials as efficient catalysts for VOCs oxidation. Mol Catal 2020;483:110766.
[59] Shamsuddin MR, Asikin-Mijan N, Marliza TS, Miyamoto M, Uemiya S, Yarmo MA, et al. Promoting dry reforming of methane via bifunctional NiO/dolomite catalysts for production of hydrogen-rich syngas. RSC Adv 2021;11:6667–81.
[60] Tsiotsias AI, Charisiou ND, AlKhoori A, Gaber S, Sebastian V, Hinder SJ, et al. Towards maximizing conversion of ethane and carbon dioxide into synthesis gas using highly stable Ni-perovskite catalysts. J CO2 Util 2022;61:102046.
[61] Madhavaram H, Idriss H, Wendt S, Kim YD, Knapp M, Over H, et al. Oxidation reactions over RuO2: a comparative study of the reactivity of the (110) single crystal and polycrystalline surfaces. J Catal 2001;202:296–307.
[62] Lux S, Baldauf-Sommerbauer G, Siebenhofer M. Hydrogenation of inorganic metal carbonates: a review on its potential for carbon dioxide utilization and emission reduction. ChemSusChem 2018;11:3357–75.
[63] Padeste C, Reller A, Oswald H-R. The influence of transition metals on the thermal decomposition of calcium carbonate in hydrogen. Mater Res Bull 1990;25:1299–305.
[64] Marasi M, Panunzi AP, Duranti L, Lisi N, Di Bartolomeo E. Enhancing oxygen reduction activity and structural stability of La0. 6Sr0. 4FeO3− δ by 1 mol% Pt and Ru B-site doping for application in all-perovskite IT-SOFCs. ACS Appl Energy Mater 2022;5:2918–28.
[65] Panunzi AP, Duranti L, Luisetto I, Lisi N, Marelli M, Di Bartolomeo E. Triggering electrode multi-catalytic activity for reversible symmetric solid oxide cells by Pt-doping lanthanum strontium ferrite. Chem Eng J 2023;471:144448.
[66] Wang Y, Paciok P, Pielsticker L, Wang W, Spriewald Luciano A, Ding M, et al. Microscopic insight into ruthenium exsolution from LaFe0. 9Ru0. 1O3 perovskite. Chem Mater 2024.
[67] Balcerzak J, Redzynia W, Tyczkowski J. In-situ XPS analysis of oxidized and reduced plasma deposited ruthenium-based thin catalytic films. Appl Surf Sci 2017;426:852–5.
[68] Morgan DJ. Resolving ruthenium: XPS studies of common ruthenium materials. Surf Interface Anal 2015;47:1072–9.
[69] Wurth W, Schneider C, Treichler R, Umbach E, Menzel D. Evolution of adsorbate core-hole states after bound and continuum primary excitation: relaxation versus decay. Phys Rev B 1987;35:7741.
[70] Qin M, Tan T, Li K, Wang Z, Yang H, Liu Z, et al. In-situ exsolved FeRu alloy nanoparticles on Ruddlesden-Popper oxides for direct hydrocarbon fuel solid oxide fuel cells. Int J Hydrogen Energy 2020;45:21464–72.
[71] Reddy GK, Quillin S, Smirniotis P. Influence of the synthesis method on the structure and CO2 adsorption properties of Ca/Zr sorbents. Energy Fuel 2014;28:3292–9.
[72] Koirala R, Gunugunuri KR, Pratsinis SE, Smirniotis PG. Effect of zirconia doping on the structure and stability of CaO-based sorbents for CO2 capture during extended operating cycles. J Phys Chem C 2011;115:24804–12.
[73] Gu W, Bousfield DW, Tripp CP. Formation of calcium carbonate particles by direct contact of Ca (OH) 2 powders with supercritical CO 2. J Mater Chem 2006;16:3312–7.
[74] López-Rodríguez S, Davo-Quinonero A, Bailón-García E, Lozano-Castello D, Bueno-Lopez A. Effect of Ru loading on Ru/CeO2 catalysts for CO2 methanation. Mol Catal 2021;515:111911.
[75] Androulakis A, Yentekakis I, Panagiotopoulou P. Dry reforming of methane over supported Rh and Ru catalysts: effect of the support (Al2O3, TiO2, ZrO2, YSZ) on the activity and reaction pathway. Int J Hydrogen Energy 2023;48:33886–902.
[76] Yentekakis IV, Goula G, Hatzisymeon M, Betsi-Argyropoulou I, Botzolaki G, Kousi K, et al. Effect of support oxygen storage capacity on the catalytic performance of Rh nanoparticles for CO2 reforming of methane. Appl Catal B Environ 2019;243:490–501.
[77] Qu P-F, Wang G-C. DFT-based microkinetic model analysis of dry reforming of methane over Ru 7/CeO 2 (111) and Ru 7/CeO 2 (110): key role of surface lattice oxygen vacancy. Catal Sci Technol 2022;12:1880–91.
[78] Liu Z, Zhang F, Rui N, Li X, Lin L, Betancourt LE, et al. Highly active ceria-supported Ru catalyst for the dry reforming of methane: in situ identification of Ruδ+–Ce3+ interactions for enhanced conversion. ACS Catal 2019;9:3349–59.
[79] Carvalho DC, de Souza HSA, Josué Filho M, Oliveira AC, Campos A, Milet ÉR, et al. A study on the modification of mesoporous mixed oxides supports for dry reforming of methane by Pt or Ru. Appl Catal Gen 2014;473:132–45.